ADVANCED FUNCTIONAL MATERIALS
www.afm-journal.de

Bioinspired Wet-Laid Electrospun Short Fiber Hybrid Networks for Aerosol Filtration

Chao Deng, Yuanqiang Xu, Juliana Martins de Souza e Silva, Hoang Thinh Nguyen, Murilo Izidoro Santos, Yu Song, Holger Schmalz, Rika Schneider, Alina Hering, Markus Langner, Ralf B. Wehrspohn, and Andreas Greiner*

The use of air filters to remove particulate matter (PM) is a crucial strategy for protecting public health. However, designing fiber-based filters often requires balancing filtration efficiency and pressure drop, which remains a significant challenge. Inspired by the microstructure of penguin feathers, this study presents a scalable and innovative wet-laid hybrid fibrous network (WHFN) air filter with a biomimetic structure. During the wet-laid process, an amphiphilic diblock copolymer (DBCP) is used to regulate the surface charge and surface energy of hydrophobic electrospun short fibers, effectively mitigating fiber aggregation in water-based processing systems. Simultaneously, electrostatic repulsion ensures that the large pores formed between coarse staple fibers are evenly partitioned by electrospun short fibers, resulting in a hybrid fibrous network structure with a uniform pore distribution. The WHFNs demonstrate excellent performance, including high filtration efficiency (91.91% for PM_1 and 100% for $PM_{2.5}$), low pressure drop (92.6 Pa), and robust mechanical strength (7.5 MPa). This work offers a simple and efficient strategy for fabricating high-performance wet-laid filters with promising applications.

1. Introduction

Atmospheric particulate matter (PM) pollution is a critical global safety concern, leading to severe environmental challenges and exerting considerable pressure on public health and the global economy.[1–3] PM is typically classified based on aerodynamic diameters into PM_{10}, $PM_{2.5}$, and PM_1, which refer to particles smaller than 10, 2.5, and 1 µm, respectively.[4–6] These airborne particles can act as carriers for various pathogenic viruses, bacteria, and toxic substances, thereby posing significant threats to public health via inhalation through the human respiratory system.[7–9] Recent outbreaks of severe respiratory diseases, including severe acute respiratory syndrome coronavirus (SARS-CoV), respiratory syncytial virus (RSV), Middle East respiratory syndrome (MERS)-CoV, and influenza virus, have highlighted the harmful effects of polluted PM.[8,10–13] Currently, the most widely accepted and recognized measures to mitigate $PM_{2.5}$ pollution include fibrous filters such as masks and air purifiers.[14–16] However, existing commercial fibrous filters, including those made from fiberglass and meltblown fibers, often demonstrate limited effectiveness in removing $PM_{2.5}$. This underscores the urgent need to develop high-performance fibrous filters suitable for commercialization to address these challenges effectively.

Fibrous filters operate by leveraging mechanisms that either passively prevent PM migration (inertial impact, sieving, interception, and diffusion) or actively capture PM (electrostatic attraction).[6,17–19] To optimize performance, achieving a balance between filtration efficiency and pressure drop is critical. This balance can be effectively managed by altering the scale of fibers or fine-tuning the porous structure of the filter, providing pathways for the development of high-performance filtration media. To enhance filtration efficiency, solution electrospinning has become a prominent research focus due to its capability to produce fibers with diameters below 1 µm and reduce filter pore sizes to the range of 2–5 µm.[20–22] Building on this, advanced strategies are being explored to develop high-performance, multifunctional filters, including adding functional additives (such as metal–organic frameworks (MOFs), graphene, silver, nano-copper and copper oxide);[23–27] charge enhancement techniques (electret,

C. Deng, H. Schmalz, R. Schneider, A. Hering, A. Greiner
Macromolecular Chemistry and Bavarian Polymer Institute
University of Bayreuth
95440 Bayreuth, Germany
E-mail: chao.deng@uni-bayreuth.de
Y. Xu
School of Textiles and Fashion
Shanghai University of Engineering Science
Shanghai 201620, China
J. M. de Souza e Silva, H. T. Nguyen, M. I. Santos, R. B. Wehrspohn
Institute of Physics
Martin Luther University Halle-Wittenberg
Heinrich-Damerow-Straße 4, 06120 Halle (Saale), Germany
Y. Song
Engineering Research Center of Technical Textiles
Ministry of Education, Donghua University
Shanghai 201620, China
M. Langner
BinNova Microfiltration GmbH
Dr.-Hermann-Ludewig-Ring 5, 07407 Rudolstadt, Germany
The ORCID identification number(s) for the author(s) of this article can be found under https://doi.org/10.1002/adfm.202511218

DOI: 10.1002/adfm.202511218

triboelectric, and piezoelectric effects);[28–31] designing innovative fiber morphologies and structures (bead-on-string, tree-like, nano-net, and cage-like structures).[32–35] These approaches aim to surpass the limitations of traditional filters and cater to modern requirements for efficiency, durability, and multifunctionality. In addition, high-performance filters have been prepared using advanced techniques such as sponge, carbon nanotube, and supramolecular nanofiber composites.[36–39] While these filters exhibit remarkable properties, challenges related to their mechanical strength, complex preparation processes, efficiency, and high production costs have hindered their large-scale commercial application. Therefore, developing efficient, simple, scalable, and cost-effective methods for producing high-performance filters is of great significance for meeting practical and commercial demands.

High-strength and high-modulus ultrafine glass fiber filters prepared using the wet-laid process have been widely commercialized since the 1970s.[40] Wet-laid technology remains a key method for preparing high-efficiency filters in industrial applications.[41–43] Its advantages are particularly evident when processing systems composed of multiple fiber types with varying properties such as diameter, length, and density. This technique enables high mixing uniformity, precise control over hierarchical structures, and effective tuning of pore architecture, making it especially suitable for the development of advanced filtration materials. However, during the wet-laid formation and drying processes, micro- and nanofibers (especially hydrophobic fibers) tend to collapse or aggregate driven by interfacial energy minimization. This aggregation results in uneven material structures, which can negatively impact the performance of the resulting filter media.[40,44] To address the issues mentioned above, various approaches have been explored to develop high-performance wet-laid filters with micro- and nanostructures. For instance, fiber aggregation has been mitigated by spraying nanofibers onto wet-laid glass fibers through vacuum-assisted filtration.[45] Although this method has successfully produced filters with excellent properties, challenges remain regarding the controllability of nanofiber distribution and the feasibility of large-scale production. In addition to vacuum-assisted filtration, other innovative techniques have been employed to enhance the performance of wet-laid filters. For example, wet-laid combined with simultaneous freeze-drying has been used to reduce pore size and improve pore uniformity.[46,47] Similarly, high-performance glass filters with tunable conformal micro/nanostructures have been prepared using freeze-drying-free ice-shellac double-template formation.[40] While these approaches yield filters with excellent performance, including high filtration efficiency, they suffer from drawbacks such as high energy consumption, low preparation efficiency, and limited scalability for industrial applications. In addition, the combination of wet-laid technology with electrospinning has been explored to prepare high-performance sandwich-structured filters.[48] While this method improves filtration performance, it still faces challenges such as low production efficiency and complex fabrication processes. Consequently, designing high-performance wet-laid filters that achieve uniform fiber distribution, controllable structure, high efficiency combined with low energy consumption (low pressure drop over the filter), and scalability remains a significant challenge.

Nature offers a plethora of hierarchical, functional structures that can be harnessed for the design of advanced filters. Inspired by the unique microfiber structure of penguin feathers,[49] we present a simple method for fabricating biomimetic fibrous filters with optimized microstructures. This approach, based on wet-laid technique, enables the creation of high-performance 3D wet-laid hybrid fibrous networks (WHFNs) that mimic the structure of penguin feathers comprising large, straight fibers and thinner fibers oriented perpendicularly to them. By blending electrospun short fibers with commercial staple fibers, and modifying the surface charge of the electrospun short fibers using a tailored, amphiphilic diblock copolymer (DBCP), 3D WHFNs with pores formed by the staple fibers and electrospun short fibers oriented perpendicularly to them were successfully prepared. The amphiphilic nature of the DBCP effectively addresses issues related to interfacial energy and surface tension during the electrospun short fiber formation process, ensuring that the pores formed between the staple fibers are uniformly divided. Additionally, due to the incorporation of montmorillonite (MT) in the electrospun short fibers, the final filter not only features a uniform hybrid fibrous network but also exhibits self-charging properties (surface potential). This unique combination enables a synergistic effect of physical screening and electrostatic attraction, enhancing the filter's ability to capture particulate matter and improve filtration performance. For oily particles such as di(2-ethylhexyl) sebacate (DEHS) with PM_1 and $PM_{2.5}$ sizes, the WHFNs achieve a filtration efficiency of 91.91% and 100%, respectively, with a pressure drop of only 92.6 Pa. When compared to the substrate without electrospun short fibers, the filtration efficiency for PM_1 and $PM_{2.5}$ is increased by 72.25% and 39.58%, respectively. Theoretical modeling and experimental results demonstrate that the high filtration performance of the filter is attributed to the uniform hybrid fibrous networks, which are formed by regulating the surface charge of the electrospun short fibers by the employed amphiphilic DBCP. In this work, we successfully developed a high-performance WHFNs filter with pores formed by the staple fibers and electrospun short fibers oriented perpendicularly to them, produced using a simple, efficient, and scalable method, showing potential for commercial application in air filtration.

2. Results and Discussion

2.1. Design and General Preparation Method of WHFNs Filter

The design of fiber-based filters often faces a critical trade-off between filtration efficiency and pressure drop, presenting a significant challenge in optimizing their performance. Drawing inspiration from the intriguing hierarchical structure of penguin downy feather, 3D WHFNs were fabricated by combining fine and coarse fibers through a hybrid approach of electrospinning and wet-laying techniques. Specifically, a polystyrene (PS) polymer solution containing montmorillonite (MT) nanosheets was employed to produce an electrospun PSMT membrane (**Figure 1a**). MT nanosheets were incorporated into the system due to their demonstrated ability to enhance the filtration efficiency of fiber-based filters.[50,51] Within the electrospun PS fibers, MT is uniformly distributed, as illustrated in Figure S1 (Supporting Information). Following electrospinning, the fiber

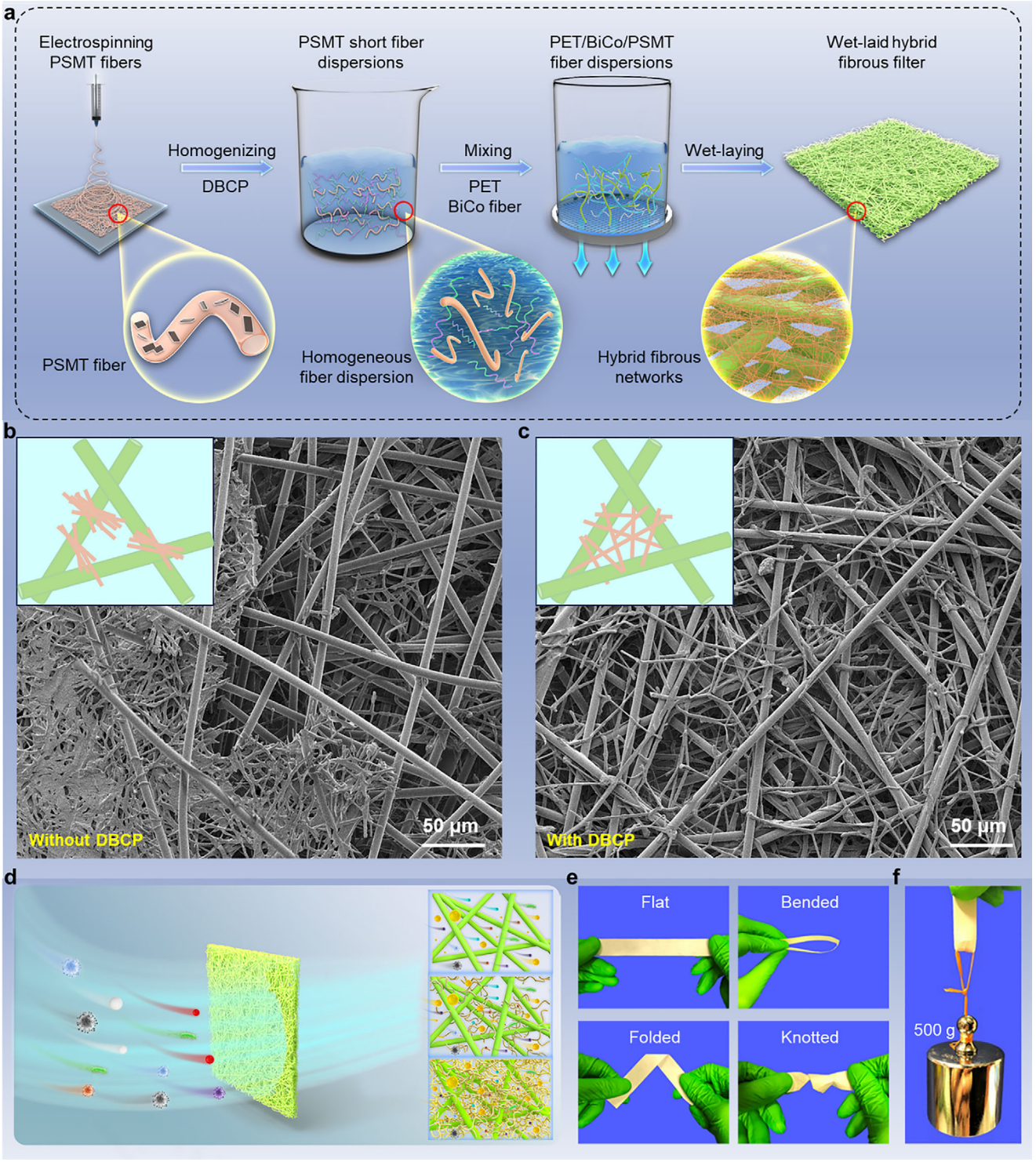

Figure 1. Structure design and fabrication of a robust WHFNs filter. a) Schematic illustration of the fabrication of WHFNs. b) SEM images of pore size segmentation by electrospun short fibers (b) without and c) with the existence of DBCP. Insets: schematic illustration of pore size segmentation of electrospun short fibers b) without and (c) in the presence of DBCP. d) Illustration of the PM filtration mechanism of the WHFNs. e) Flexibility of the WHFNs. f) Robust mechanical properties of the WHFNs.

membrane was mechanically cut into short fibers, employing a method previously established by our group.[52] Notably, the length of electrospun PSMT short fibers can be precisely controlled by adjusting the cutting time, as demonstrated in Figure S2 (Supporting Information). The electrospun PSMT short fibers were then dispersed into a uniform fiber dispersion with the assistance of an amphiphilic poly(acrylic acid)-*block*-poly(*n*-butyl acrylate) (PAA_{100}-*b*-P*n*BA_{57}) diblock copolymer (DBCP). Importantly, in the absence of DBCP, the PSMT short fibers tend to aggregate severely (Figure 1b), leading to an uneven fiber distribution within the network (Figure 1c). The dispersion was subsequently mixed with commercial poly(ethylene terephthalate) (PET) and bicomponent (BiCo) staple fibers, the latter serving as a binder due to their lower melting point mantle. The mixture was processed using wet-laid forming technology to fabricate hybrid fibrous networks, followed by hot pressing at 130 °C to produce the final high-performance WHFNs filter (Figure S3, Supporting Information). It is noteworthy that the electrospun short fibers can be prepared independently in an offline manner, while the remaining raw materials are commercially available. Moreover, the process relies on water-based dispersion and low-temperature drying, making the overall wet-laid approach highly compatible with roll-to-roll manufacturing and offering significant potential for large-scale industrial implementation. Due to the three-dimensional hybrid fibrous network structure of the prepared filter, the electrospun short fibers effectively divide the large pores formed by the coarse staple fibers, creating a fibrous network with a more uniform pore size distribution with smaller pores. This structural design enables the efficient capture of target PM while maintaining a low pressure drop across the filter (Figure 1d). Moreover, WHFNs exhibit excellent flexibility (Figure 1e; Movie S1, Supporting Information) and robust mechanical properties (Figure 1f), facilitating its integration with other equipment for practical applications.

2.2. Formation of WHFNs

Hydrophobic polymer fibers present significant challenges in achieving uniform dispersions during water-based processing, primarily due to interfacial energy or surface tension, which often leads to fiber aggregation and results in uneven material structures that compromise the final performance. Similarly, the electrospun PSMT fibers prepared in this study face comparable processing challenges after being cut into short fibers (**Figure 2**a), owing to their hydrophobic nature, as evidenced by a water contact angle of 136° (Figure S4, Supporting Information). To address this issue, we first synthesized an amphiphilic diblock copolymer (DBCP) (Method S1, Supporting Information), composed of hydrophilic poly(acrylic acid) (PAA) and hydrophobic poly(*n*-butyl acrylate) (P*n*BA) blocks (Figure 2b). By increasing the pH of the solution, the acrylic acid groups within the polymer chain can be deprotonated (Figure S5, Supporting Information), thereby modulating the molecular chain conformation of the DBCP in solution (pK_a (PAA) = 5.4).[53] When the electrospun PSMT short fibers are dispersed in the DBCP aqueous solution (pH ≈ 8.5), the hydrophobic P*n*BA segments of the DBCP adsorb onto the surface of the PSMT short fibers via hydrophobic interactions, while the hydrophilic PAA segments orient themselves toward the aqueous phase (Figure 2c). This effectively addresses the challenge of dispersing hydrophobic PSMT short fibers in aqueous solution. Notably, we demonstrated both directly and indirectly that the DBCP can adsorb onto the surface of PS using quartz crystal microbalance measurements (Figure S6, Supporting Information) and water contact angle experiments (Figure S7, Supporting Information), respectively. As a result, the DBCP adsorbs on the surface of the PSMT short fibers and prevents aggregation due to the electrostatic repulsion of the negatively charged PAA segments, leading to the formation of a uniformly dispersed fiber dispersion (Figure 2d). In particular, the change in zeta potential values before and after the addition of DBCP to the PSMT short fiber dispersion further confirms the enhancement of surface charge on the PSMT fibers (Figure S8, Supporting Information). This increased surface charge promotes stronger electrostatic repulsion between the fibers, facilitating the uniform dispersion of PSMT short fibers when they are mixed with PET and BiCo fiber dispersions for wet-laid formation. This results in the formation of a 3D hybrid fibrous network structure with PET and BiCo fibers, characterized by a uniform pore size distribution (Figure 2e). Interestingly, the shear viscosity of the PSMT short fiber dispersion with DBCP is significantly reduced compared to that of the neat PSMT short fiber dispersion at the same fiber concentration (Figure S9, Supporting Information). Furthermore, photographs of the fiber dispersions taken after the shear viscosity tests revealed distinct differences. In the absence of DBCP, the fibers formed numerous entangled and aggregated bundles due to shear forces. In contrast, the fibers in the DBCP-containing dispersion remained uniformly dispersed (Figure S9, Supporting Information). These findings demonstrate that the DBCP effectively prevents the aggregation of hydrophobic polymer fibers under various shear forces encountered during processing.

Based on the above findings, we proceeded to fabricate the WHFN filters. To ensure uniform fiber formation and maximize the MT content, a PS concentration of 24 wt.% and an MT content of 4 wt.% were selected for the preparation of PSMT short fibers. These parameters were identified as optimal based on a comparison of electrospinning results across varying PS and MT concentrations (Note S1, Supporting Information). Hereafter, PSMT refers to the short fibers prepared with PS (24 wt.%) and MT (4 wt.%) unless otherwise stated. The average diameter and length of the prepared PSMT short fibers are 2.05 ± 0.47 and 192.9 ± 98.6 µm, respectively (Figure S10, Supporting Information). Their surface morphology is presented in SEM images and optical microscopy images (Figure S10, Supporting Information). PSMT short fibers in varying proportions (wt.% relative to PET and BiCo (9/1 w/w) fibers) were mixed with PET and BiCo fibers, and the WHFNs were fabricated using the wet-laid process. Specifically, the as-fabricated wet-laid hybrid fibrous network filters are referred to as WHFNs-x-y, where x and y refer to the use of DBCP and the percentages of PSMT short fibers, respectively. SEM images of the top surface of the WHFNs revealed that the PSMT short fibers were uniformly distributed as their proportion increased (Figure 2f–l). Additionally, the large pores formed between PET and BiCo fibers were progressively subdivided into smaller, more uniformly distributed pores. This unique hybrid fibrous network structure might enhance the ability of WHFNs to effectively capture PM, while minimizing the

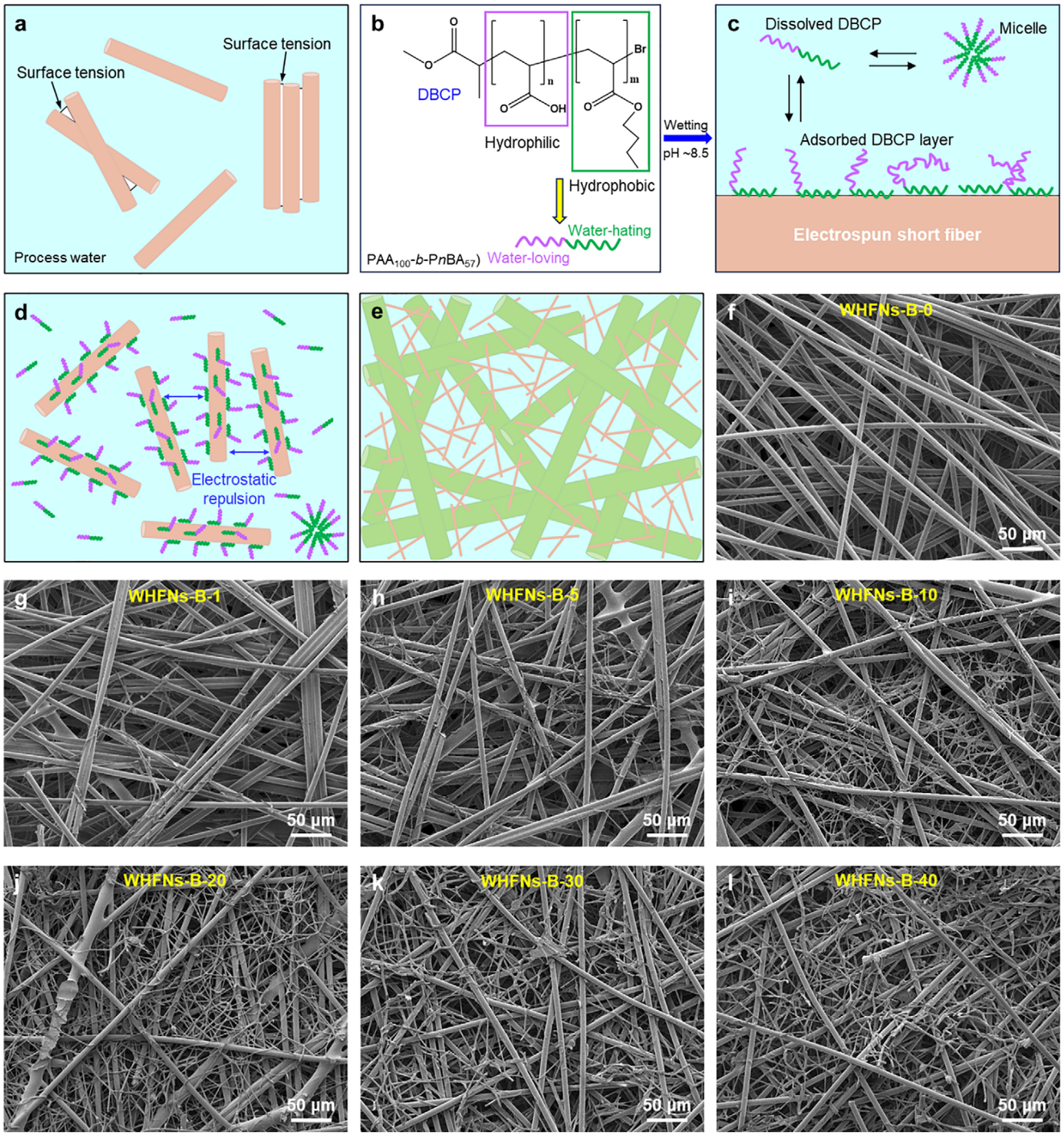

Figure 2. Formation of WHFNs. a) Agglomeration of electrospun PSMT short fibers in process water. b) Structure of DBCP. c) Wetting mechanism of PSMT short fiber by adsorption of DBCP. Schematic depiction of d) a homogeneous electrospun PSMT short fiber dispersion with DBCP addition, and e) segmentation of pore size by PSMT short fibers. f–l) SEM images of WHFNs with different percentages of PSMT short fibers.

pressure drop over the filter. Furthermore, SEM images of the bottom surface of the WHFNs demonstrate that, as the proportion of PSMT short fibers increases, the bottom surface exhibits a similar fibrous network structure with pore segmentation, consistent with the top surface (Figure S11, Supporting Information). These findings indicate that PSMT short fibers are uniformly distributed throughout the entire cross-section of the WHFNs during the wet-laid process. To further investigate the fiber distribution, the cross-sections of the WHFNs were analyzed. As expected, PSMT short fibers were found to be evenly distributed among the PET and BiCo fibers (Figure S12, Supporting Information). This well-integrated 3D hybrid fibrous network

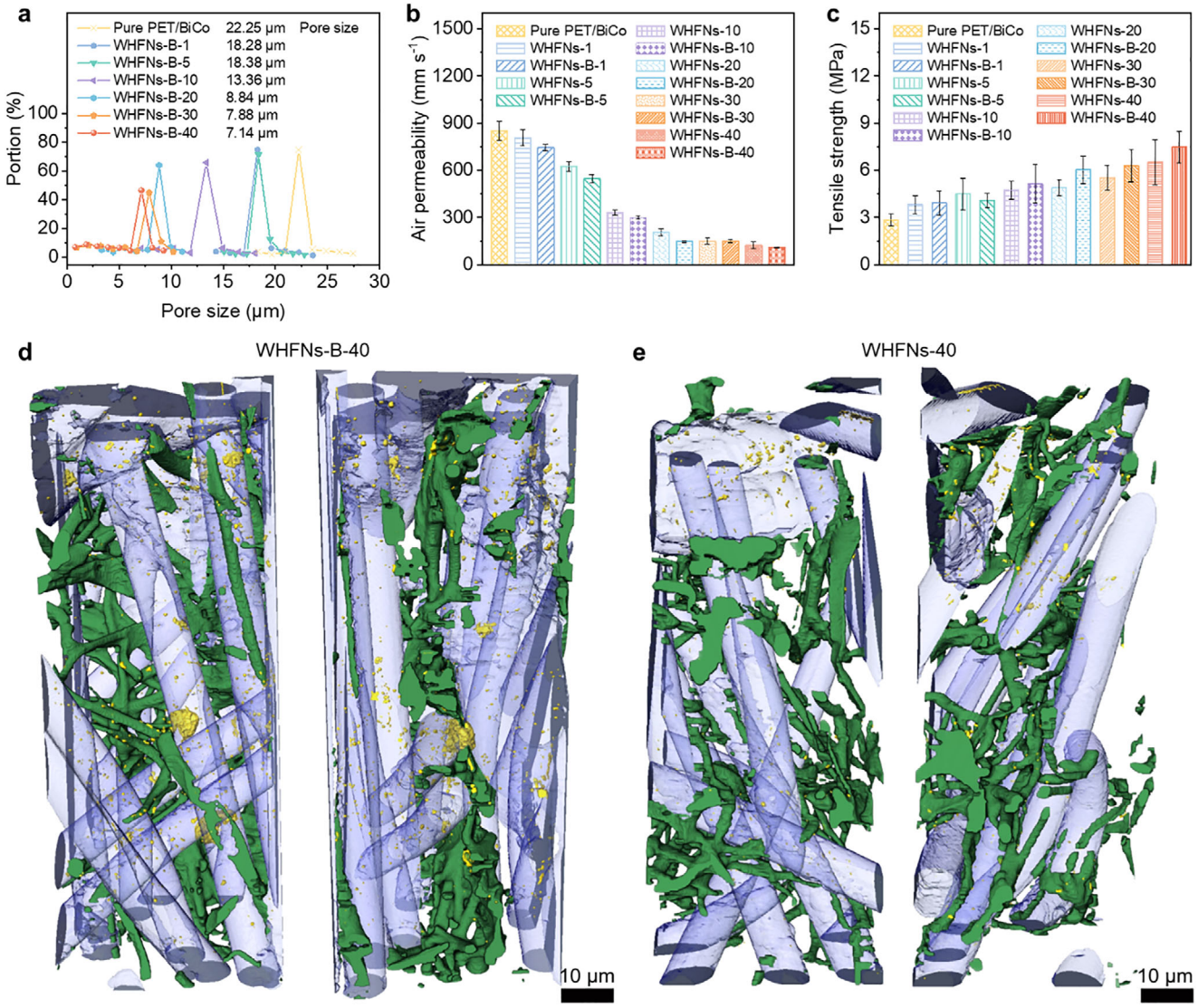

Figure 3. Structure characteristics of WHFNs. a) Pore size distributions of WHFNs with DBCP. b) air permeability and c) tensile strength of WHFNs with different percentages of PSMT short fibers. X-ray microscopy images of fiber volumetric distributions of d) WHFNs-B-40 and e) WHFNs-40.

structure is anticipated to provide robust support for the WHFNs filter during the continuous interception of PM.

To verify the hypothesis that the DBCP can effectively facilitate the uniform dispersion and distribution of hydrophobic PSMT short fibers, WHFNs were also prepared without DBCP. SEM images clearly show that the distribution of PSMT short fibers becomes highly uneven, with significant fiber aggregation in some regions and sparse distribution in others, as their proportion increases (Figure S13, Supporting Information). Consequently, the fiber material fails to form a fibrous network with uniform pore distribution. This uneven structure suggests that the overall performance of the WHFNs without DBCP in capturing PM would be significantly compromised. Interestingly, two commercially available ionic surfactants, anionic sodium dodecyl sulfate (SDS) and cationic cetyltrimethylammonium bromide (CTAB), were also used to disperse the fibers and prepare filter materials via the wet-laid process. However, under identical processing conditions, the resulting filter materials exhibited significantly less uniform structures compared to those prepared with DBCP (Figure S14, Supporting Information). These results further highlight the superiority of DBCP over conventional ionic surfactants in promoting uniform fiber dispersion and regulating the resulting microstructure of the filter material.

2.3. Structure Characteristics of WHFNs

Based on the prepared WHFNs, their structures and physical properties were systematically analyzed. As shown in **Figure 3a**, the average pore diameter of the WHFNs decreases progressively with increasing proportions of PSMT short fibers. Specifically, WHFNs-B-40 exhibited a concentrated pore size of 7.14 μm, representing a 68% reduction compared to the pore size (22.25 μm) of the pure PET/BiCo substrate without PSMT short fibers. This

demonstrates that the introduction of finer PSMT short fibers effectively reduces the pore size of the pure PET/BiCo substrate, thereby enhancing filtration performance. Interestingly, a comparison of the pore sizes of WHFNs prepared with and without DBCP during the wet-laid process reveals that the average pore sizes of WHFNs with DBCP are slightly smaller and more consistent than those without DBCP (Figure S15, Supporting Information). This further confirms that the DBCP enhances the uniformity of the pore size distribution within the WHFNs. X-ray microscopy (XRM) illustrates the volumetric distribution of large staple fibers and PSMT short fibers, and the WHFNs prepared with and without the existence of DBCP (Figure 3d,e). The images corroborate with the observations above and show that in the presence of DBCP the organization and alignment of the large staple fibers have a more ordered and compact arrangement. In the absence of DBCP, the PSMT short fibers are more agglomerated resulting in a structure with more open pores compared to the DBCP containing counterpart. In terms of air permeability, the pure PET/BiCo substrate exhibits a permeability of 851 mm s^{-1} under the pressure difference of 200 Pa, while WHFNs-B-40 shows a reduced air permeability of 108 mm s^{-1} (Figure 3b). Furthermore, as the proportion of PSMT short fibers increases, the tensile strength of the WHFNs also improves significantly. For instance, the tensile strength of WHFNs-B-40 reaches 7.5 MPa, which is more than twice the value for the pure PET/BiCo substrate (2.8 MPa) (Figure 3c). These results highlight that the incorporation of short fibers markedly enhances the mechanical properties of the WHFNs filter, making it suitable for practical applications.

In order to further characterize the internal structure of the WHFNs filters and visualize the 3D structure of the filters, volumetric images obtained with XRM was used. The volumetric distribution of the large staple fibers, the PSMT short fibers including the distribution of the MT within it was visualized in all WHFNs filters (Figure S16, Supporting Information). The porosity of the WHFNs calculated from the volumetric images varied from 58.8% to 86.8% (Table S1, Supporting Information). The observed differences from expectation are due to the field of view of XRM being relatively small compared to the overall size of the filters, and it does not capture their full complexity, as they are heterogeneous at the microscale.

2.4. Filtration Performance of WHFNs Filter

Figure 4 systematically presents the filtration performance of the WHFNs filters. Oily particles of DEHS with various particle size distributions were selected as a model for PM filtration (Figure S17, Supporting Information). Figure 4a illustrates the filtration efficiency of WHFNs with varying proportions of PSMT short fibers under an airflow velocity of 5.33 cm s^{-1}. The filtration efficiency of the WHFNs increases steadily with the proportion of PSMT short fibers. Specifically, the PET/BiCo substrate achieves filtration efficiencies of 60.42% and 19.66% for $PM_{2.5}$ and PM_1, respectively. In contrast, the WHFNs-B-40 exhibits significantly improved filtration efficiencies of 100% for $PM_{2.5}$ and 91.91% for PM_1, corresponding to increases of 39.58% and 72.25%, respectively. Notably, when the proportion of PSMT short fibers reaches 20% or higher, the WHFNs with DBCP demonstrate superior filtration efficiencies, particularly for smaller PM, compared to those without DBCP. For instance, WHFNs-B-20 achieves filtration efficiencies of 81.80% for PM_1 and 41.22% for $PM_{0.3}$, whereas WHFNs-20 exhibits filtration efficiencies of only 66.93% for PM_1 and 31.62% for $PM_{0.3}$, respectively. These results further confirm that the DBCP facilitates the uniform distribution of PSMT short fibers, promoting the formation of a consistent pore structure during the wet-laid process and thereby enhancing the overall performance of WHFNs.

The filtration performance of WHFNs at a high airflow velocity (18.85 cm s^{-1}) was also investigated (Figure 4b). Interestingly, unlike conventional fiber-based filters, which typically exhibit diminished performance at higher airflow velocities, the filtration efficiency of WHFNs for larger PM increased with rising airflow velocity (Figure 4b). For instance, the filtration efficiencies of WHFNs-B-20, WHFNs-B-30, and WHFNs-B-40 were 95.55%, 95.10%, and 98.01% for PM_1, respectively. In comparison, at an airflow velocity of 5.33 cm s^{-1}, the filtration efficiencies for PM_1, were 81.80%, 92.90%, and 91.91%, respectively (Figure 4a). These unique characteristics may be attributed to the triboelectric properties of the WHFNs. Numerous studies have reported that the adsorption efficiency of ultrafine particulate matter can be enhanced through electrostatic attraction, particularly by harnessing surface electrostatic charges generated via friction between two materials (i.e., triboelectricity).[54–56] Incorporating MT into the fiber matrix has been shown to enhance the triboelectric performance of polymer-based materials, facilitating the continuous accumulation of surface charges on the fiber network and thereby improving filtration efficiency.[50] Consequently, the hybrid fibrous network structure of WHFNs can remove PM not only through physical sieving but also by enhancing particle capture via electrostatic adsorption, enabled by triboelectric effects (Figure 4c). This dual mechanism significantly boosts filtration efficiency, particularly under higher airflow velocities, where triboelectric charging further contributes to the effective capture of fine particles. In addition, the electrostatic adsorption capability of WHFNs was confirmed through surface potential measurements during both discharging and recharging processes (Figure S18, Supporting Information). The strong electrostatic attraction on the WHFNs surface was further visually validated by the effective adsorption of fine carbon particles, demonstrating their enhanced capacity for capturing airborne particulates (Figure S18, Supporting Information).

Regarding the pressure drop performance of the WHFNs, Figure 4c shows that although the pressure drop tends to increase with the proportion of PSMT short fibers, WHFNs-B-30 and WHFNs-B-40 still maintain relatively low pressure drops of 84.4 and 92.6 Pa. This is likely attributed to the uniform pore size distribution in WHFNs with DBCP, which allows for an even distribution of airflow and prevents excessive local pressure buildup. These findings further validate the role of DBCP in facilitating the formation of a uniform fibrous network during the wet-laid process. The pressure drops of the WHFNs exhibited a trend similar to that observed at low airflow velocity, increasing with the proportion of PSMT short fibers (Figure 4d). Specifically, the WHFNs-B-40 filter showed a pressure drop of 371.1 Pa. However, given the enhanced filtration efficiency, a lower PSMT fiber ratio, such as 30%, can be employed to achieve a more balanced performance. For example, the WHFNs-B-30 filter achieved a pressure

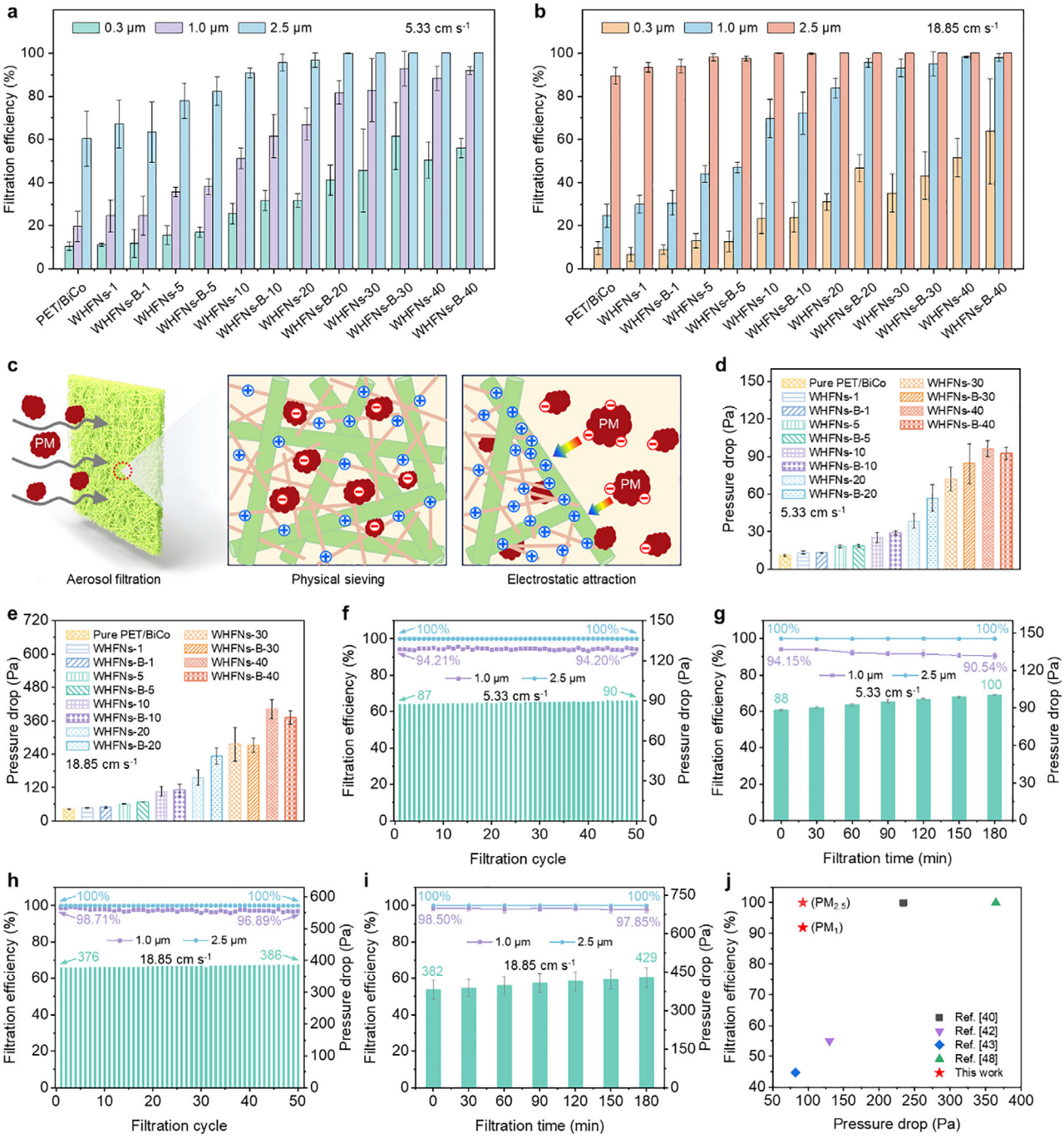

Figure 4. Filtration performance of WHFNs. Filtration efficiency of WHFNs with different percentages of PSMT short fibers under an airflow velocity of a) 5.33 cm s^{-1} (9 L min^{-1}) and b) 18.85 cm s^{-1} (32 L min^{-1}). c) Schematic diagram of filtration mechanism. Pressure drop of WHFNs with different percentages of PSMT short fibers under an airflow velocity of d) 5.33 cm s^{-1} (9 L min^{-1}) and e) 18.85 cm s^{-1} (32 L min^{-1}). f) Filtration efficiency and pressure drop of WHFNs-B-40 with 50 filtration cycles (5.33 cm s^{-1}). g) Long-term filtration of WHFNs-B-40 (5.33 cm s^{-1}). h) Filtration efficiency and pressure drop of WHFNs-B-40 with 50 filtration cycles (18.85 cm s^{-1}). i) Long-term filtration of WHFNs-B-40 (18.85 cm s^{-1}). j) Comparison of DEHS filtration efficiency and pressure drop of WHFNs and previously reported wet-laid filters.

drop of only 272.6 Pa, providing an optimal trade-off between filtration efficiency and pressure drop.

The quality factor (QF) is a critical parameter for evaluating the overall performance of filter materials (Figure S19, Supporting Information). At an airflow velocity of 5.33 cm s^{-1}, the overall trend shows that the QF of WHFNs increases with the rising proportion of PSMT fibers, except in the case of WHFNs-B-40. This deviation may be attributed to the relatively high pressure drop at higher PSMT content, which results in a comparatively lower QF despite the improved filtration efficiency.

Interestingly, when examining the QF of WHFNs at high airflow velocity (18.85 cm s^{-1}) (Figure S20, Supporting Information), it was observed that the QF of WHFNs exhibits an increasing trend with the rising proportion of PSMT fibers when filtering PM_1. However, for $PM_{2.5}$ filtration, the QF shows a trend of first increasing and then decreasing, with WHFNs-B-10 achieving the highest QF value (0.106 Pa^{-1}). Notably, WHFNs with higher percentages of PSMT fibers (e.g., 30% and 40% PSMT short fibers) showed excellent filtration efficiency, however, their increased pressure drop resulted in lower QF values especially when filtering PM with larger sizes. This finding provides valuable guidance for the practical application of these filters, emphasizing the importance of balancing filtration efficiency and pressure drop to optimize performance under specific operating conditions.

Additionally, the service life of the prepared WHFNs was evaluated through repeated filtration tests. After 50 filtration cycles at an airflow velocity of 5.33 cm s^{-1}, the filtration efficiency for $PM_{2.5}$ and PM_1 remained virtually unchanged, while the pressure drop exhibited only a slight increase (Figure 4e). Following a 3 h continuous filtration test (Figure 4f), the PM_1 filtration efficiency of the WHFNs filter decreased slightly from 94.15% to 90.54%, while the $PM_{2.5}$ filtration efficiency remained at 100%. Impressively, the pressure drop only increased by 12 Pa. The service life of the WHFNs was also evaluated under high airflow velocity (18.85 cm s^{-1}). After 50 filtration cycles, the filtration efficiency for PM_1 only slightly decreased, while the filtration efficiency for $PM_{2.5}$ remained stable at 100% (Figure 4g). Concurrently, the pressure drop increased by only 10 Pa. Regarding the long-term filtration performance, the filtration efficiency is as excellent as the performance in the 50-cycle filtration, despite an increase in pressure drop from 382 to 429 Pa (Figure 4h). The observed increase in pressure drop is likely attributed to pore blockage caused by the accumulation of PM within the porous structure of the WHFNs filter during prolonged filtration. These results demonstrate the excellent filtration durability and extended service life of the WHFNs filter. Moreover, our designed hybrid fibrous network structure enables WHFNs filter to achieve high filtration efficiency with relatively lower pressure drop, making it competitive with other wet-laid filters (Figure 4j; Table S2, Supporting Information).

In addition, to further evaluate the stability of WHFNs filters after long-term storage and exposure to high-humidity environments, the filtration performance of WHFNs-B-40 was tested after 135 days of storage and after being placed in an environment with 75% relative humidity for 12 h (Figure S21, Supporting Information). The results show that both the filtration efficiency and pressure drop remained nearly identical to those of freshly prepared WHFNs-B-40, with only a slight decrease in filtration efficiency observed for relatively small DEHS particles. These findings highlight the excellent environmental stability and durability of the WHFNs filters.

Furthermore, dust filtration measurements were conducted to better evaluate the performance of WHFNs under practical environmental conditions (Figure S22, Supporting Information). Compared to their performance in DEHS filtration, both WHFNs-B-20 and WHFNs-B-40 exhibited higher filtration efficiencies across various particle sizes, suggesting that WHFNs may possess superior dust removal capabilities relative to DEHS particles. Taking into account both pressure drop and quality factor values, WHFNs-B-20 appears to offer a more favorable balance of performance, making it more suitable for dust filtration applications than WHFNs-B-40.

2.5. CFD Simulation of the Filtration Media

To gain deeper insights into the airflow and particle transport characteristics within the WHFNs, numerical simulations were conducted on the airflow field and particle motion field during filtration. For comparison, pure PET/BiCo and WHFNs with varying percentages of PSMT short fibers were selected. The simulations were conducted using COMSOL Multiphysics 6.3. The 3D model of the sample was constructed based on the parameters of the prepared WHFNs, including fiber diameter, sample thickness, and porosity (Table S3, Supporting Information). The calculation domain and boundary conditions of the sample unit are illustrated in Figure S23 (Supporting Information). Based on the filtration test, the inlet air velocity was set at 5.33 cm s^{-1}.

Figure 5a presents the pressure fields simulated for five different filter models. At a uniform surface velocity of 5.33 cm s^{-1}, the highest pressure is observed on the upper surface of all five models, while the pressure gradually decreases with increasing sample depth (i.e., distance from the upper surface). The pressure drop of the sample is determined by the pressure difference between the upper and lower surfaces of the model. The pressure increase along the *z*-axis for different models was quantitatively recorded, illustrating the decreasing trend of air pressure with increasing depth within the nonwoven structure (Figure 5c). The simulated pressure drops for pure PET/BiCo, WHFNs-B-10, WHFNs-B-20, WHFNs-B-30, and WHFNs-B-40 were ≈30, 101, 148, 270, and 394 Pa, respectively (Figure 5d). Hence, the pressure difference in the filter models increases with the PSMT percentage, indicating that a higher content of PSMT short fibers results in a greater pressure drop in the filter. This trend aligns well with the experimental results. Notably, the pressure drop predicted by the simulation is higher than that measured in the experiments, with the discrepancy becoming more pronounced as the proportion of PSMT fibers increases. Due to the complexity and computational demands of model construction, certain factors have been appropriately simplified: i) Fiber orientation in the model is restricted to the *x*-*y* plane, with no alignment in the z direction. ii) The surface morphology of the fibers is not considered, and they are represented as smooth cylinders. iii) The fiber network is modeled as a uniform, idealized porous structure, which does not fully capture the irregular and heterogeneous pore distribution in the real sample. iv) No fiber deformation or membrane compressibility is considered, while in reality, the membrane may slightly deform under flow pressure, reducing effective resistance. v) The model assumes steady-state, single-phase laminar flow with fixed boundary conditions, neglecting possible fiber-fiber gaps or slip effects at the micro scale. These factors may contribute to the discrepancies between the simulated and experimental results. Nevertheless, the consistency in trend between the two provides valuable insights for future filter design.

Additionally, simulations of particle motion for different particle sizes (0.3, 1.0, and 2.5 μm) within the filter model were conducted to predict the PM capture efficiency. In these simulations,

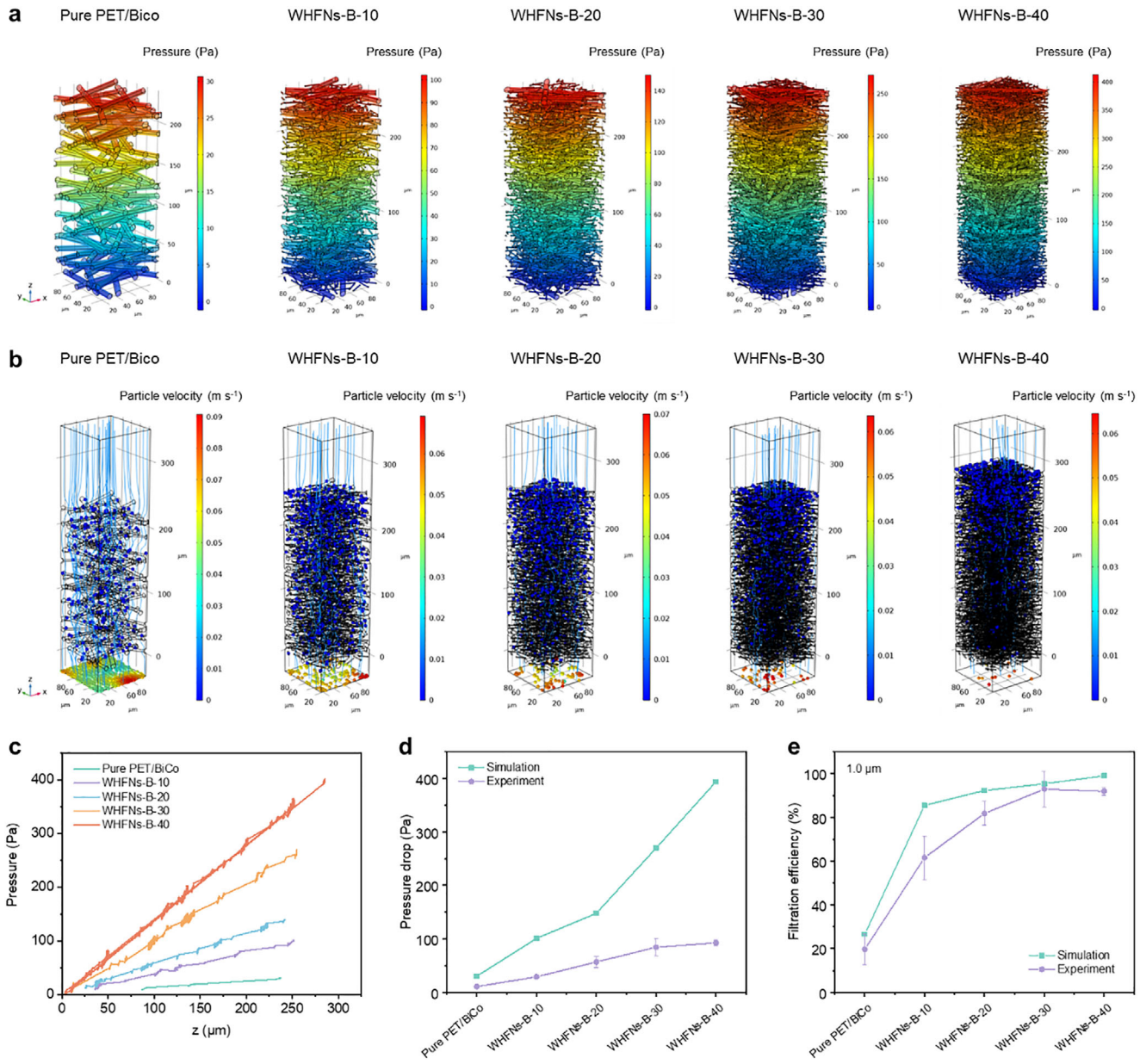

Figure 5. CFD simulation of the filtration media. 3D diagrams of a) the pressure field and b) the particle velocity field when the air flow passes through the inside of pure PET/BiCo and WHFNs. The blue particles in b) represent those that have been captured, and the particles in different colors represent those that have escaped. c) Pressure variation along the *z*-axis of pure PET/BiCo and WHFNs. Comparison of d) pressure drops and e) filtration efficiencies for pure PET/BiCo and WHFNs in real experimental measurement and CFD simulation.

it is assumed that particles are captured upon contact with the fibers. At the entrance of the computational domain, 1000 particles with a diameter of 1.0 μm were introduced at the same velocity as the airflow (Figure 5b). The filtration efficiency was determined by calculating the percentage of captured particles relative to the total number of particles introduced.

Figure 5b presents the particle velocity fields for the five models. In the pure PET/BiCo model, many particles retain a certain velocity after passing through the filter, indicating its limited particle capture capability. As the PSMT percentage increases, the particle capture efficiency of WHFNs improves progressively. Notably, in the WHFNs-B-40 model, the velocity of most particles rapidly decreases to 0, with nearly all particles being captured near the upper surface, demonstrating significantly enhanced filtration performance. For the simulations of 0.3 and 2.5 μm particle motion, the model indicates that the trend in particle trapping ability with varying PSMT percentages is consistent with the results observed for 1.0 μm particles (Figure S24, Supporting Information). Furthermore, a comparison between the simulation results and the experimentally measured filtration efficiency is presented in Figure 5e, revealing a consistent trend between the two, further validating the predictive reliability of the simulation.

Based on the simulation results, an appropriate PSMT percentage can be selected to optimize filter performance, achieving a desirable balance between filtration efficiency and pressure drop for various application scenarios.

3. Conclusion

We introduced a facile, efficient, and scalable strategy for the fabrication of high-performance filter materials. By employing an amphiphilic DBCP to modify the surface charge and surface energy of hydrophobic electrospun short fibers, the aggregation of these fibers in a water-based processing system was significantly reduced. Additionally, the adsorption of the DBCP onto the fiber surfaces induces electrostatic repulsion, enabling the short fibers to effectively partition the large pores formed between PET/BiCo coarse fibers. As a result, a hybrid fibrous network structure with smaller, more uniformly distributed pores was formed, enhancing the overall filtration performance. Due to our structural design, the WHFNs demonstrated outstanding performance, including high filtration efficiency (91.91% for PM_1 and 100% for $PM_{2.5}$), low pressure drop (92.6 Pa), excellent mechanical strength (7.5 MPa), and long-term stability. Both theoretical modeling and experimental results confirmed that the hybrid fibrous network structure facilitated the capture of PMs. This study offers valuable insights for the design of high-performance wet-laid filters, promoting their broader application in environmental protection, energy, and related fields.

4. Experimental Section

Materials: PET (poly(ethylene terephthalate)) fibers with 0.5 dtex thickness and 5 mm cutting length (Advansa, Germany) and bicomponent staple fibers (6 mm, 2.2 dtex) with a melting point of 110 °C (271p, Advansa, Germany) were selected as raw materials for wet-laid formation. Polystyrene (M_W = 192 000, and ρ = 1.04 g cm^{-3}, Sigma–Aldrich), *N,N'*-dimethylformamide (DMF, ≥99.8%, Sigma–Aldrich), acetone (ACS reagent, ≥99.5%, Sigma–Aldrich), montmorillonite (682659-500G, Sigma–Aldrich), sodium dodecyl sulfate (A1502-1000G, AppliChem GmbH, Germany), cetyltrimethylammonium bromide (52370-500G, Fluka), isopropanol (tech.) and other laboratory-grade chemicals were used as received without further purification. Poly(acrylic acid)-*block*-poly(*n*-butyl acrylate) diblock copolymer (DBCP) was synthesized and more details were provided in the Supporting Information.

Electrospinning of PSMT Fibers: Polystyrene was dissolved with different weight concentrations in a solvent mixture of DMF and acetone (70/30 w/w) by magnetic stirring for 5 h. Separately, montmorillonite (MT) nanoclay was sonicated in an ultrasound bath for 2 h in the solvent mixture (2.5–10.0 wt.%). Later, the PS solution and the MT nanoclay suspension were mixed to form a PSMT suspension with a concentration of 21–27 wt.% of PS and 1–4 wt.% of MT, and sonicated for another 2 h to obtain homogeneous and stable suspensions for electrospinning. A volume of 4 mL of the PSMT precursor suspension was placed in a 5 mL syringe with a stainless-steel needle. Electrospinning was conducted at a feed rate of 0.6 mL h^{-1} under an applied voltage of 15–20 kV with a distance of 15 cm between the needle tip and the collector, which was covered with baking paper to ease the collection of the electrospun membranes obtained (ambient conditions: ≈23 °C and ≈50% RH). Detailed electrospinning parameters are listed in Table S3 (Supporting Information).

Cutting of PSMT Short Fibers: Pieces of the electrospun PSMT membrane were added to 1.5 L of a water-isopropanol mixture (2/1 v/v) in a *Robot Coupe Blixer 6*. The fiber-solvent mixture was cooled using liquid nitrogen until a slurry formed and the PSMT short fibers suspension was obtained at different cutting times at the fastest speed of 3500 rpm. Liquid nitrogen was repeatedly added in between to keep the suspension cool and slurry-like. Afterward, DBCP was added for stabilization of the dispersion that will be used for wet-laid formation.

Fabrication of WHFNs: The steps to fabricate wet-laid hybrid fibrous networks (WHFNs) involved dispersing PET fibers and bicomponent (BiCo) fibers (9/1 w/w) in deionized water with agitation for ≈15 min (400 rpm) using a mechanical stirrer. Then, the PSMT short fiber dispersion was added and mechanically stirred for an additional 3 min. The prepared mixed fiber slurry was poured into a plastic column of 20 cm-diameter with a steel mesh placed at the base of the column for wet-laid formation, and the final fiber concentrations were between 0.21 and 0.29 g L^{-1}. The WHFNs were formed on the steel mesh when the water was filtered out. The as-prepared WHFNs were then placed in a heating plate to remove the remaining water. Finally, the WHFNs were consolidated by a hot-pressing device, applying a pressure of 1.5 MPa for 6 min at 130 °C.

DEHS and Dust PMs Filtration Performance: A filter test station (Palas MFP 2000, Germany) was utilized for the filtration measurement. The test aerosol used in the experiment was microparticles of di(2-ethylhexyl) sebacate (Palas DEHS) and dust with different sizes. Reliable determination of the aerosol concentration and the particle size, and therefore an accurate determination of the fraction separation efficiency, could be ensured with the aid of the light scattering spectrometer Promo 2000 (Palas, Germany). The samples with an effective testing area of 28.3 cm^2 were measured under different continuous airflow velocities of 5.33 and 18.85 cm s^{-1}, respectively. The quality factor (QF, Pa^{-1}) of the sample was calculated by the equation,

$$QF = \frac{\ln(1-\eta)}{\Delta p} \tag{1}$$

where η is the filtration efficiency and Δp (Pa) is the pressure drop.

Characterization: Flow curves of the electrospun PSMT short fiber dispersions with and without DBCP were measured on a MCR302 rheometer (Anton Paar, Austria) equipped with a double gap cylinder system (DG26.7). Measurements were conducted at 23 °C employing a shear rate range of 0.1–100 s^{-1}. The pore size was measured with a TOPAS PSM 165/H porometer with a measurement area of 0.95 cm^2 and TOPOR (density: 1.9 g cm^{-3}; surface tension: 16.0 mN m^{-1}) as the test liquid. Scanning electron microscopy (SEM, FEI Quanta FEG 250) was used to characterize the surface morphology of the electrospun short fibers and WHFNs. The elemental distributions of samples were investigated by energy dispersive X-ray spectroscopy (EDS) mapping (JSM-7600F SEM, Hitachi). Optical images of the electrospun short fibers were obtained by a digital optical microscopy (Smartzoom 5, Carl Zeiss). Mechanical properties of the samples were measured by a tensile testing machine (ZwickiLine Z0.5, Zwick/Roell, Germany). The fluorescence tests of microplastic suspension containing Rhodamine were performed on a spectrofluorometer (FP-8600, Jasco) equipped with a rectangular cell holder for solutions (light path 10 mm). Electrostatic field tester (EFM 023, Kleinwaechter GmbH, Germany) was used to measure the surface potential of filters. The zeta potential of samples was detected by Zetasizer Ultra (Malvern, Germany).

Supporting Information

Supporting Information is available from the Wiley Online Library or from the author.

Acknowledgements

The authors acknowledge the financial support of the German Federal Ministry of Education and Research (BMBF) for the BMBF-funded project "Pinguin" under grant number 13XP5180A, in collaboration with which this work was developed. Chao Deng thanks the Alexander von Humboldt Foundation for financially supporting his postdoctoral fellowship,

and thanks Alexander Kern for helping conducting the air filtration experiments. The authors gratefully acknowledge the use of equipment and assistance offered by the Keylab "Small Scale Polymer Processing" and by the Keylab "Electron- and Optical Microscopy" of the Bavarian Polymer Institute at the University of Bayreuth.

Conflict of Interest

The authors declare no conflict of interest.

Data Availability Statement

The data that support the findings of this study are available in the supplementary material of this article.

Keywords

bioinspired, electrospinning, filtration, polymer, wet-laid

Received: May 5, 2025
Revised: July 14, 2025
Published online: July 24, 2025

[1] S. Rajagopalan, R. D. Brook, P. R. Salerno, B. Bourges-Sevenier, P. Landrigan, M. J. Nieuwenhuijsen, T. Munzel, S. V. Deo, S. Al-Kindi, *Lancet Diabetes Endocrinol.* **2024**, *12*, 196.
[2] C. Li, A. van Donkelaar, M. S. Hammer, E. E. McDuffie, R. T. Burnett, J. V. Spadaro, D. Chatterjee, A. J. Cohen, J. S. Apte, V. A. Southerland, *Nat. Commun.* **2023**, *14*, 5349.
[3] Z. Zhou, X. Shuai, Z. Lin, X. Yu, X. Ba, M. A. Holmes, Y. Xiao, B. Gu, H. Chen, *Lancet Planet. Health* **2023**, *7*, 649.
[4] T. Sigsgaard, B. Hoffmann, *Science* **2024**, *384*, 33.
[5] M. C. Turner, Z. J. Andersen, A. Baccarelli, W. R. Diver, S. M. Gapstur, C. A. Pope, III, D. Prada, J. Samet, G. Thurston, A. Cohen, *CA: Cancer J. Clin.* **2020**, *70*, 460.
[6] H. Liu, Y. Zhu, C. Zhang, Y. Zhou, D. G. Yu, *Nano Today* **2024**, *55*, 102161.
[7] Y. Zhang, Y. Han, X. Ji, D. Zang, L. Qiao, Z. Sheng, C. Wang, S. Wang, M. Wang, Y. Hou, *Nature* **2022**, *610*, 74.
[8] C. C. Wang, K. A. Prather, J. Sznitman, J. L. Jimenez, S. S. Lakdawala, Z. Tufekci, L. C. Marr, *Science* **2021**, *373*, abd9149.
[9] Y. Yang, X. Li, Z. Zhou, Q. Qiu, W. Chen, J. Huang, W. Cai, X. Qin, Y. Lai, *Nat. Commun.* **2024**, *15*, 1586.
[10] P. V. Markov, M. Ghafari, M. Beer, K. Lythgoe, P. Simmonds, N. I. Stilianakis, A. Katzourakis, *Nat. Rev. Microbiol.* **2023**, *21*, 361.
[11] S. Choi, E. M. Kim, S. Y. Kim, Y. Choi, S. Choi, N. Cho, H. J. Park, K. K. Kim, *Environ. Pollut.* **2022**, *315*, 120439.
[12] P. G. da Silva, M. S. J. Nascimento, R. R. Soares, S. I. Sousa, J. R. Mesquita, *Sci. Total Environ.* **2021**, *764*, 142802.
[13] C. Deng, F. Seidi, Q. Yong, X. Jin, C. Li, X. Zhang, J. Han, Y. Liu, Y. Huang, Y. Wang, *J. Hazard. Mater.* **2022**, *424*, 127391.
[14] M. Zhou, S. Zhang, H. Guo, X. Zhou, J. Xu, Q. Luo, X. Li, Q. Xu, C. Xiong, R. Wang, *Adv. Mater.* **2025**, *37*, 2419389.
[15] H. Liu, J. Shi, Y. Liang, S. Zhou, Y. Liu, Y. Liu, X. Chen, D. Yu, *Adv. Mater.* **2025**, *37*, 2419143.
[16] C. Deng, F. Seidi, Q. Yong, X. Jin, C. Li, L. Zheng, Z. Yuan, H. Xiao, *J. Adv. Res.* **2022**, *39*, 147.
[17] S. Shi, W. Bai, X. Chen, Y. Si, C. Zhi, H. Wu, Y. Su, W. Cai, B. Fei, C. W. Kan, *Adv. Funct. Mater.* **2025**, 2423284.
[18] Z. Peng, J. Shi, X. Xiao, Y. Hong, X. Li, W. Zhang, Y. Cheng, Z. Wang, W. J. Li, J. Chen, *Nat. Commun.* **2022**, *13*, 7835.
[19] F. Seidi, C. Deng, Y. Zhong, Y. Liu, Y. Huang, C. Li, H. Xiao, *Small* **2021**, *17*, 2102453.
[20] A. Greiner, J. H. Wendorff, *Angew. Chem., Int. Ed.* **2007**, *46*, 5670.
[21] Z. Yu, T. Fan, Y. Liu, L. Li, J. Liu, B. Yang, S. Ramakrishna, Y. Z. Long, *Sep. Purif. Technol.* **2024**, *499*, 127773.
[22] Z. Shao, Q. Wang, Z. Gui, R. Shen, R. Chen, Y. Liu, G. Zheng, *Sep. Purif. Technol.* **2024**, *358*, 130417.
[23] X. He, C. Wang, Y. Hao, J. Li, G. Zhu, L. Jiang, J. Shao, M. Zhang, X. P. Li, H. Li, *ACS Appl. Mater. Interfaces* **2024**, *16*, 54873.
[24] J. Liu, E. Tian, S. Zhang, D. Kong, K. Liu, X. Bai, K. Liu, *Adv. Fiber Mater.* **2023**, *5*, 461.
[25] P. Lyu, Z. Ju, J. Hu, H. Pan, X. Li, Y. Liu, J. Ren, B. Shang, X. Liu, W. Xu, *Adv. Funct. Mater.* **2024**, *34*, 2400685.
[26] G. Zhou, G. Chen, Y. Xin, J. Pang, J. Wang, L. Jiang, R. Liu, *Adv. Funct. Mater.* **2024**, *35*, 2419533.
[27] F. Hadinejad, H. Morad, M. Jahanshahi, A. Zarrabi, H. Pazoki-Toroudi, E. Mostafavi, *Adv. Fiber Mater.* **2023**, *5*, 1273.
[28] Q. Wang, Y. Wei, W. Li, X. Luo, X. Zhang, J. Di, G. Wang, J. Yu, *Angew. Chem., Int. Ed.* **2021**, *60*, 23756.
[29] M. K. Kisomi, S. Seddighi, R. Mohammadpour, A. Rezaniakolaei, *Nano Energy* **2023**, *112*, 108514.
[30] S. Shi, Y. Si, Z. Li, S. Meng, S. Zhang, H. Wu, C. Zhi, W. F. Io, Y. Ming, D. Wang, *ACS Nano* **2023**, *17*, 7035.
[31] M. Yang, X. Li, N. Yao, J. Yu, X. Yin, S. Zhang, B. Ding, *ACS Nano* **2024**, *18*, 16895.
[32] Y. Yang, W. Wang, M. Zhong, Y. Gou, N. Lu, Y. Cheng, T. Zhu, J. Huang, W. Cai, Y. Lai, *Chem. Eng. J.* **2024**, *495*, 153245.
[33] W. Zhao, M. Wang, Y. Yao, Z. Cheng, Y. Shen, Y. Zhang, J. Tao, J. Xiong, H. Cao, D. Zhang, *Macromol. Rapid Commun.* **2024**, *45*, 2300685.
[34] M. Yang, X. Gong, S. Wang, Y. Tian, X. Yin, X. Wang, J. Yu, S. Zhang, B. Ding, *Nano Lett.* **2023**, *23*, 10579.
[35] F. Wang, Y. Si, J. Yu, B. Ding, *Adv. Funct. Mater.* **2021**, *31*, 2107223.
[36] J. Zhu, R. Zhu, Y. Hu, Z. Wang, *Sep. Purif. Technol.* **2023**, *305*, 122445.
[37] J. Xiong, A. Li, Y. Liu, L. Wang, X. Qin, J. Yu, *Small* **2022**, *18*, 2105570.
[38] D. Schröder, K. Kreger, H. W. Schmidt, *ACS Appl. Mater. Interfaces* **2025**, *17*, 14569.
[39] W. Sun, S. Dong, M. Gao, H. Diao, Y. Song, L. Zhang, H. Wang, D. Yuan, *Macromol. Rapid Commun.* **2025**, *46*, 2401019.
[40] Z. Zhou, T. You, D. Wang, Z. Pan, G. Xu, Y. Liang, M. Tang, *Adv. Funct. Mater.* **2024**, *34*, 2306777.
[41] M. Langner, A. Greiner, *Macromol. Rapid Commun.* **2016**, *37*, 351.
[42] Z. Sun, M. Tang, Q. Song, J. Yu, Y. Liang, J. Hu, J. Wang, *Cellulose* **2018**, *25*, 6719.
[43] Y. Yao, S. Liu, T. You, Z. Zhou, X. Zhang, M. Tang, Z. Sun, J. Wang, J. Hu, *Sep. Purif. Technol.* **2022**, *295*, 121263.
[44] Y. Hu, Z. Lao, B. P. Cumming, D. Wu, J. Li, H. Liang, J. Chu, W. Huang, M. Gu, *Proc. Natl. Acad. Sci.* **2015**, *112*, 6876.
[45] Y. Xiong, J. Cai, Z. Wu, R. Zheng, L. Wang, D. Wang, X. Wang, *ACS Appl. Mater. Interfaces* **2024**, *16*, 52799.
[46] J. Nie, J. Liao, T. Jiao, B. Sun, M. Zhang, R. Yang, Y. Li, *Chem. Eng. J.* **2024**, *500*, 156719.
[47] J. Liao, J. Nie, B. Sun, T. Jiao, M. Zhang, S. Song, *Chem. Eng. J.* **2024**, *482*, 148908.
[48] D. Atalie, Z. X. Chen, H. Li, C. G. Liang, M. C. Gao, X. X. Cheng, P. C. Ma, *J. Hazard. Mater.* **2024**, *478*, 135608.
[49] M. Burgard, D. Weiss, K. Kreger, H. Schmalz, S. Agarwal, H. W. Schmidt, A. Greiner, *Adv. Funct. Mater.* **2019**, *29*, 1903166.
[50] Y. Cho, Y. Son, J. Ahn, H. Lim, S. Ahn, J. Lee, P. K. Bae, I. D. Kim, *ACS Nano* **2022**, *16*, 19451.
[51] Y. Cai, Q. Yang, E. Wang, Y. Liang, W. Han, Y. Miao, J. Huang, W. Zhang, *Appl. Surf. Sci.* **2024**, *657*, 159737.

[52] G. Duan, S. Jiang, V. Jérôme, J. H. Wendorff, A. Fathi, J. Uhm, V. Altstädt, M. Herling, J. Breu, R. Freitag, *Adv. Funct. Mater.* **2015**, *25*, 2850.
[53] O. Colombani, M. Ruppel, F. Schubert, H. Zettl, D. V. Pergushov, A. H. Müller, *Macromolecules* **2007**, *40*, 4338.
[54] A. Vázquez-López, X. Ao, J. S. del Río Saez, D. Y. Wang, *Nano Energy* **2023**, *114*, 108635.
[55] S. Cha, Y. Cho, J. G. Kim, H. Choi, D. Ahn, J. Sun, D. s. Kang, C. Pak, J. J. Park, *Small Methods* **2022**, *6*, 2101545.
[56] Y. Liu, S. Zheng, M. Wang, X. Zhang, F. Wang, J. Yu, X. Hu, J. Lin, Y. Liu, *J. Hazard. Mater.* **2025**, *495*, 138793.